Performance Evaluation of a Novel Photovoltaic-electrochemical Hybrid System

Qin Zhao [1], Xinru Guo [1], Houcheng Zhang [1, *], Meng Ni [2], Shujin Hou [3, *]

[1] *Department of Department of Microelectronic Science and Engineering, Ningbo University,*

Ningbo 315211, China

[2] *Department of Building and Real Estate, The Hong Kong Polytechnic University, Hong Kong,*

China

[3] *College of Physics and Electronic Engineering, Nanyang Normal University, Nanyang 473061,*

China

Abstract: To harvest the relatively high wavelength sunlight, a novel hybrid system coupling a

thermally regenerative electrochemical cycle to a dye-sensitized solar cell is proposed. Efficiencies

and power outputs of dye-sensitized solar cell and thermally regenerative electrochemical cycle are

calculated, and the mathematical relationship between the electric current of thermally regenerative

electrochemical cycle and the working current density of dye-sensitized solar cell is deduced. The

power output and efficiency of the hybrid system are also derived considering multiple irreversible

losses. The feasibility and effectiveness of the proposed hybrid system will be assessed by

comparing the performances between the hybrid system and the single dye-sensitized solar cell.

Numerical calculations show that the maximum efficiency and power density of the hybrid system

allow 32.04% and 32.18% greater than that of the single dye-sensitized solar cell, respectively.

Comprehensive parametric studies are undertaken to examine the dependences of the hybrid system

performance on some operating conditions and microstructure parameters, including electrode

porosity, photoelectron absorption coefficient, Schottky barrier, film thickness and internal resistance

22   of thermally regenerative electrochemical cycle. The derived results may offer new insights into

23   design and optimization of such an actual hybrid system.

24

27   * Corresponding authors. zhanghoucheng@nbu.edu.cn (H. Zhang); houshujingrb@163.com (S.

28   Hou).

29

1. Introduction

Energy shortage and environmental pollution are two major challenges of the 21st century. So far, fossil fuels are still playing the most important role in the global energy structure. With the growth of the world population and economic development, it is a global consensus to vigorously promote the energy revolution by replacing fossil fuels by renewable energies, such as wind energy, biomass energy, geothermal energy, wave energy and solar energy [1]. Herein, solar energy is the most potential alternative to meet the increasing clean energy demand because it is abundant, free and clean. Solar energy can be actively used through photovoltaic cell, solar thermal system and concentrated solar power system [2]. Photovoltaic cells enable direct conversion of the solar energy into electricity without any intermediate energy conversion processes. Photovoltaic cells have made a great progress in the past 30 years and can be mainly classified into organic, inorganic and hybrid solar cells [3].

As one kind of organic solar cells, dye-sensitized solar cells (DSSCs) convert visible light into electricity using dye molecules for light absorption. Then, the excited dye molecules inject electrons into the titanium dioxide (TiO_2), which subsequently conducts the electrons to the current collector. DSSCs have unique advantages such as abundant raw materials, low cost, simple technology and achievable large-scale industrialized production [4]. In addition, all raw materials and production process are non-toxic and non-polluting, and a part of the materials can be fully recycled. For DSSCs, considerable studies have been carried out both theoretically and experimentally [5] on some aspects, including sensitizer development [6], photo electrode fabrication [7], prototype design [8] and performance modeling [9].

However, the present energy conversion efficiency of DSSCs is not adequately high, and up to 80% of the absorbed energy is wasted into the surroundings due to the interfacial transference, relaxation and recombination losses. The energy conversion efficiency can be also enhanced if the relatively high wavelength sunlight is collected and recovered for combined cooling, heating and power (CCHP) applications. For example, Su et al. [10] proposed a hybrid device consisting of DSSC and semiconductor thermoelectric refrigerator to harvest solar energy for cooling. Pounraj et al. [11] experimentally studied a novel Peltier based hybrid photovoltaic/thermal (PV/T) active solar still to increase the freshwater yield and to improve the efficiency of the solar PV panel. Prince Winston et al. [12] further investigated a hybrid PV/T active still incorporating a Nickel-Chromium (NiCr) heater to increase the production of distillate water and enhance the PV efficiency. Owing to the relatively low operating temperature, most of the available researches have focused on photovoltaic-thermoelectric (PVTE) hybrid systems [13], which apply thermoelectric generators (TEGs) to reuse the waste heat from photovoltaic cells for extra electrical power generation [14]. For instance, Babu et al. [15] presented a novel PVTE system and found that overall efficiency of PV-TEG system was 6% higher than that of the sole PV. Wang et al. [16] created a PVTE hybrid device and found that the overall energy conversion efficiency of the hybrid device was 13% greater than that of the single DSSC. Xu et al. [17] demonstrated a PVTE hybrid device that integrated the hole-conductor-free perovskite solar cell based on a TiO_2/Zirconium dioxide (ZrO_2)/carbon structure PV and a TEG. Under the irradiation of 100 mW cm^{-2}, the optimized hybrid device achieved a maximum efficiency of 20.3% and an open-circuit voltage (OCV) of 1.29V. Kil et al. [18] fabricated a concentrating PVTE hybrid device consisting of a single-junction GaAs-based solar cell and a TEG,

72   and their hybrid generator gave rise to the conversion efficiency by about 3% compared to the single

73   concentrating photovoltaic cell. Yin et al. [19] studied the coupling selection principle and optimal

74   design methods for a concentrating PVTE hybrid system. Yin et al. [20] also evaluated the feasibility

75   of a photovoltaic-thermoelectric-thermal cogeneration system and found that the energy efficiency

76   and exergy efficiency were, respectively, 43.06% and 31.43%. Mahmoudinezhad et al. [21]

77   investigated the transient response of a hybrid system comprised of a concentrated PV cell and a

78   TEG. Park et al. [22] tried to fully use the spectrum solar energy via coupling TEGs to harness the

79   waste heat from thermalization and transmission losses from PV cell. Their method found that the

80   overall conversion efficiency was 30% under a 15°C temperature gradient. Bjørk et al. [23]

81   compared the maximum efficiencies between a hybrid system that the TEG was directly mounted on

82   the PV back and a tandem system that the short and long wavelength sunlight were sent to PV and

83   TEG, respectively. The maximum increases in efficiency for the combined case and tandem case

84   were found to be 4.5% and 1.8%, respectively.

85   As an alternative heat-to-electricity device, a thermally regenerative electrochemical cycle

86   (TERC) constructs a thermodynamic cycle using the temperature-dependence of electrochemical cell

87   voltages [24]. An electrochemical cell is charged at a temperature with lower voltage and then

88   discharged at a different temperature with higher cell voltage, thereby converting heat into electricity

89   by varying temperature [25]. TREC is regarded as a promising low-grade heat harvesting technology

90   because of its high efficiency [26], high temperature coefficient and low cost [27]. Recently, TRECs

91   have attracted much attention in the scientific community [28]. Long et al. have evaluated the

92   performances of TREC using objective functions such as power output and efficiency [29],

93   ecological [30] as well as maximum power output and exergy efficiency [31]. Wang et al. [32]

94   optimized a low-grade heat driven TREC with continuous power output using the maximum

95   efficiency-power product criterion. Guo et al. [33] studied the performance of an upgraded TREC

96   considering the external heat leakage, heat transfer irreversibility and non-ideal regeneration losses.

97   Lee et al. [25] demonstrated an efficient TREC based on the thermogalvanic effect for harvesting

98   low-grade heat energy. Yang et al. [34] fabricated a novel charging-free TREC, and the

99   heat-to-electricity conversion efficiency of 2.0 % could be reached for the TREC operating between

100 20 °C and 60 °C. Yang et al. [35] also reported a membrane-free TREC with a nickel

101 hexacyanoferrate (NiHCF) cathode and a silver/silver chloride anode. In addition to the studies on

102 TREC itself, some studies have used TREC to harness the waste heat from low-temperature power

103 sources. For example, Long et al. [36] and Zhang et al. [37] have integrated the TERC with proton

104 exchange membrane fuel cell (PEMFC) and alkaline fuel cell (AFC) for waste heat harvesting, and

105 found that the performances of the hybrid systems are better than that of the single fuel cells [38].

106 However, seldom research has been reported on using TREC to harvest the waste heat from

107 photovoltaic cells.

108   To fill the research gap, a novel photovoltaic-electrochemical hybrid system is proposed by

109 integrating a DSSC and a TREC, where the TREC harvests the waste heat from the DSSC for further

110 electric power generation. Considering various irreversible losses within DSSC and TREC as well as

111 between them, the performances of DSSC, TREC and proposed system will be theoretically derived

112 and studied. The electric current relationship between DSSC and TREC will be derived. The

113 feasibility and effectiveness of the proposed approach will be illustrated by comparing the

114 performances between the proposed system and the single DSSC. Moreover, the effects of the film

115 thickness of electrode material, porosity, Schottky barrier, photoelectron absorption coefficient and

116 internal resistance of TREC on the proposed system performance will be discussed in detail.

117 **2. System description**

118 As depicted in Fig. 1, the proposed hybrid system is composed of a transparent DSSC, a solar

119 selective absorber (SSA) [39] and a TREC, where the SSA is placed between the DSSC and the

120 TREC, and the DSSC and the TREC are electrically connected in series. The DSSC converts the

121 short wavelength sunlight (smaller than 920 nm) into electricity [40], while the relatively high

122 wavelength sunlight not utilized by the DSSC (larger than 920 nm) is absorbed by the SSA and then

123 converted into heat energy [41]. The SSA is a carbon nanotube-based tandem one, which acts as

124 near-perfect blackbody absorber with the thickness larger than 10 μm [42]. The carbon nanotubes

125 have good optical properties (i.e., absorptance and emittance close to 1), high thermal stability (i.e.,

126 they exhibit thermal stability at 580 °C in vacuum for 30 days) and high thermal conductivity (>3000

127 W m^{-1} K^{-1}) [42], which enable rapid heat transfer from the SSA (< 60 °C) to the TREC for electricity

128 generation. Therefore, the performance of the proposed hybrid system is expected to be better than

129 that of a single DSSC. In Fig. 1, **Error! Reference source not found.** is the power output of DSSC;

130 P_{TREC} is the power output of TREC; Q_{2n} is the heat flow from SSA to TREC; Q_{1n} is the heat flow

131 lost to the environment from TREC; Q_L is the rate of heat leakage from the DSSC into the

132 environment; T is the DSSC operating temperature; T_e is the environment temperature; T_1 and

133 T_2 are, respectively, the heat-sink and heat-source temperatures of the TREC.

134 To simplify the subsequent analyses with accuracy, the following assumptions are adopted:
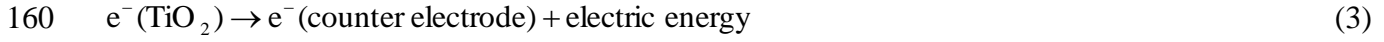
135   (1) All inlet wavelength sunlight is fully utilized [43];

136   (2) Zero energy losses from the SSA to the environment due to the small temperature difference

137   between the SSA and the environment [39];

138   (3) Transport of carriers in semiconductor is governed by diffusion motion due to the negligibly

139   small drift motion [10];

140   (4) Diffusion length of carriers is constant since the carriers have an average lifetime [10];

141   (5) The heat-source temperature of TREC is equal to the operating temperature of DSSC because the

142   SSA has high thermal conductivity [44];

143   (6) The heat-sink temperature of TREC is equal to the ambient temperature [44];

144   (7) The charging time is equal to the discharging time for the TREC [32].

145   It should be pointed out that the above assumptions are widely used in the current literatures, and the

146   influences of these assumptions on the hybrid system performance are negligibly small.

147   **2.1. Dye-sensitized solar cell**

148   The DSSC main structure is based on a semiconductor formed between an electrolyte and a

149   photo-sensitized anode. The detailed working processes of DSSC can be briefly described as follows

150   [45]. When sunlight irradiates the porous nano-TiO_2 thin film, the dye molecules absorb photons and

151   then generate electrons. The generated electrons are injected to TiO_2 and transported from the

152   nano-TiO_2 thin film to the external electrical load, as described by Eq. (1) $\sim$ Eq. (3) [46].

153   Afterwards, electrons move through an external electric circuit to the counter electrode from which

154   electrons are transferred to the redox electrolyte. The oxidized dye is restored by extra electron to

155   regenerate Iodide, and the Iodide is going to be oxidized into tri-iodide, as described in Eq. (4) [46].

156   In the end, the tri-iodide keeps travelling through the electrolyte until it arrives the counter electrode

157   to get the lost electron, as described by Eq. (5) [46].

158     $\Theta + \text{photon} \rightarrow \Theta^*$ (1)

159     $\Theta^* + \text{TiO}_2 \rightarrow e^-(\text{TiO}_2) + \Theta^+$ (2)

160     $e^-(\text{TiO}_2) \rightarrow e^-(\text{counter electrode}) + \text{electric energy}$ (3)

161     $\Theta^+ + \frac{3}{2}\text{I}^- \rightarrow \Theta + \frac{1}{2}\text{I}_3^-$ (4)

162     $\frac{1}{2}\text{I}_3^- + e^-(\text{counterelectrode}) \rightarrow \frac{3}{2}\text{I}^-$ (5)

163   Since electron transfer in the nano-TiO$_2$ thin films is mainly governed by diffusion, one can

164   effectively simulate the performance of DSSC by establishing electron diffusion model [47]. Under

165   steady-state conditions, the generation, transport [48] and recombination [49] of electrons in DSSC

166   can be described by

167     $D\dfrac{\partial^2 n(x)}{\partial x^2} - \dfrac{n(x) - n_0}{\tau^*} + \Phi\alpha e^{-\alpha x} = 0$ (6)

168   where x is the coordinate starting from the TiO$_2$/transparent conducting oxide (TCO) interface;

169     $n(x)$ is the excessive electron concentration at x; n_0 is the electron concentration under a dark

170   condition; τ^* is the electron lifetime; Φ is the light intensity; α is the light absorption

171   coefficient of the electrode; D is the electron diffusion coefficient.

172   With the boundary conditions (i.e., Eq. (7) and Eq. (8)), the short-circuit current density J_{sc}

173   [50] can be obtained by solving Eq. (6), as shown by Eq. (9) [51]

174     $n(0) = n$ (7)

175     $(dn/dx)_{x=d} = 0$ (8)

176 $$J_{sc} = \frac{q\Phi_0 L\alpha \left[-L\alpha \cosh\left(\frac{d}{L}\right) + \sin\left(\frac{d}{L}\right) + L\alpha \exp(-d\alpha) \right]}{(1 - L^2\alpha^2)\cosh\left(\frac{d}{L}\right)} \qquad (9)$$

177 where

178 $$L = \sqrt{D\tau^*} \qquad (10)$$

179 is the electron diffusion length; Φ_0 is the light intensity at 1 sun condition; q is the charge of an

180 electron; d is the thickness of the thin film.

181   Neglecting the losses at the interface between electrode and electrolyte, the photovoltage of the

182 DSSC is given by [50]

183 $$V = V_0 - V_1 \qquad (11)$$

184 where V_0 is the difference of the redox potential between the electrolyte and the TiO_2 Fermi level;

185 V_1 is the voltage loss at the TiO_2/TCO interface.

186   The potential difference V_0 can be expressed as

187 $$V_0 = \frac{kTm^{\#}}{q} \ln\left[\frac{(J_{sc} - J)L\cosh\left(\frac{d}{L}\right)}{qDn_0 \sinh\left(\frac{d}{L}\right)} + 1 \right] \qquad (12)$$

188 where $m^{\#}$ is the ideality factor, k is the Boltzmann constant.

189   Referring to the thermionic-emission theory, the voltage loss at the TiO_2/TCO interface can be

190 calculated by

191 $$J = A^* T^2 \exp\left(\frac{-q\Phi_b}{kT}\right)\left[\exp\left(\frac{qV_1}{kT}\right) - 1\right] \qquad (13)$$

192 where

193 $$A^* = \frac{4\pi m^* q k^2}{h^3} \tag{14}$$

194 is the Richardson constant of TiO$_2$; h is the Planck constant; m^* is equal to 5.6 times the electron

195 mass for TiO$_2$; Φ_b is the Schottky barrier height.

196   Rearranging Eq. (13), the voltage loss can be further expressed as

197 $$V_1 = \frac{kT}{q} \ln\left[1 + \frac{J}{A^* T^2 \exp\left(-\frac{q\Phi_b}{kT}\right)} \right] \tag{15}$$

198   Substituting Eq. (12) and Eq. (15) into Eq. (11), the photovoltage of DSSC can be calculated as

199 $$V = \frac{kTm^\#}{q} \ln\left[\frac{(J_{sc} - J)L\cosh\left(\frac{d}{L}\right)}{qDn_0 \sinh\left(\frac{d}{L}\right)} + 1 \right] + \frac{kT}{q} \ln\left[1 + \frac{J}{A^* T^2 \exp\left(-\frac{q\Phi_b}{kT}\right)} \right] \tag{16}$$

200   With the help of Eq. (13) and Eq. (16), the power output and efficiency of the DSSC can be,

201 respectively, given by

202 $$P_D = VJA_D \tag{17}$$

203 $$\eta_D = \frac{P_D}{GA_D} = \frac{VJ}{G} \tag{18}$$

204 where G is the solar irradiation under 1 sun condition; A_D is the effective area of the DSSC.

205   Since the internal recombination reaction and diffusion process [52] of DSSC are very sensitive

206 to temperature changes [53], the influence of operating temperature on the DSSC performance must

207 be taken into account. Considering the effects of operating temperature, the deviations of the power

208 output and efficiency can be, respectively, given by

209 $$P_{dev} = \lambda\left(T - T_{ref}\right) \tag{19}$$

210 $$\eta_{dev} = \beta\left(T - T_{ref}\right) \tag{20}$$

211 where λ and β are, respectively, the decreasing rates of the power output and efficiency with

212 respect to the DSSC operating temperature; and β is interrelated with λ. When λ is 0.00506

213 mW K^{-1}, the theoretical results of power output density fit well with the experimental results in Ref.

214 [54]. Similarly, according to Eq. (15) ~ Eq. (18) and Ref. [55], β can be calculated as 0.0114 K^{-1}.

215 Therefore, Eq. (17) and Eq. (18) should be, respectively, modified into

216 $$P_D = VJA_D - \lambda\left(T - T_{ref}\right) \tag{21}$$

217 $$\eta_D = \frac{VJ}{G}\left[1 - \beta\left(T - T_{ref}\right)\right] \tag{22}$$

218 **2.2. Thermally regenerative electrochemical cycle**

219 TREC within the hybrid system consists of n TREC elements, which can generate a continuous

220 power output in the temperature range of 293 ~ 333 K [34]. The positive electrode of a TREC

221 element is made of solid copper hexacyanoferrate ($CuHCF$) immersed in sodium nitrate ($NaNO_3$)

222 aqueous solution and the negative electrode is made of metal copper (Cu) immersed in 3 M copper

223 nitrate ($Cu\,NO_{3\,2}$) aqueous solution. The positive and negative electrodes are separated by an

224 anion membrane [25]. The relevant electrochemical reactions at the cathode and anode are,

225 respectively, $Na_{0.71}Cu\left[Fe^{III}(CN)_6\right]_{0.72} + a\left(Na^+ + e^-\right) = Na_{0.71-a}Cu\left[Fe^{III}(CN)_6\right]_{0.72-a} + \left[Fe^{II}(CN)_6\right]_{0.72+a}$

226 and $Cu^{2+} + 2e^- = Cu$ [32]. The TREC elements can be divided into three parts [29]: one part

227 functions as hot cells that tightly contact with the hot reservoir, i.e., the SSA; another part works as

228 cold cells that tightly contact with the cold reservoir, i.e., the environment; and the rest part conducts

229 the regenerative processes.

230 In the charging progress, the produced heat is totally released to the hot reservoir. In the

231 discharging process, the produced heat is totally released to the cold reservoir. The heat absorbed

232　from the hot reservoir at temperature T_2 and the heat released to the cold reservoir at temperature

233　T_1 during the isothermal processes can be, respectively, expressed as

234　$$q_2^* = \alpha_c T_2 C_q \tag{23}$$

235　$$q_1^* = \alpha_c T_1 C_q \tag{24}$$

236　where α_c is the temperature coefficient; C_q is the charge capacity.

237　　　The heat released to the hot reservoir and the heat dissipated into the cold reservoir during the

238　two isothermal processes can be, respectively, expressed as

239　$$q_{J1}^* = I_{ch}^2 R t_{ch} \tag{25}$$

240　$$q_{J2}^* = I_{dis}^2 R t_{dis} \tag{26}$$

241　where I_{ch} and I_{dis} are the electric currents of the charging process and discharging process,

242　respectively; R is the electric resistance; t_{ch} is the time of charging process; t_{dis} is the time of

243　discharging process.

244　　　The regenerative losses in a cycle is given by [30]

245　$$q_{RL}^* = (1 - \eta_{RL}) C_p (T_2 - T_1) \tag{27}$$

246　where η_{RL} is the regenerative efficiency; C_p is the heat capacity.

247　　　Thus, the heat absorbed from the hot reservoir [32] and the heat released to the cold reservoir

248　[56] during the cycle time for a TREC element can be, respectively, expressed as

249　$$Q_2^* = \alpha_c T_2 C_q - I_{ch}^2 R t_{ch} + (1 - \eta_{RL}) C_p (T_2 - T_1) \tag{28}$$

250　$$Q_2^* = \alpha_c T_1 C_q - I_{dis}^2 R t_{dis} + (1 - \eta_{RL}) C_p (T_2 - T_1) \tag{29}$$

251　　　The cycle time of the TREC, τ, satisfies the following relations

252　$$\tau = t_{ch} + t_{dis} + t_r \tag{30}$$

253      $n\, t_{ch} = m\, \tau$ (31)

254   where $t_{ch} = C_q / I_{ch}$; n is the number of TRECs; m is the number of the cells charging

255   simultaneously [57].

256   When $m \geq 2$, both m and n should satisfy two relations: (1) $n/m \geq 2$, and (2) $n/m \neq N$

257   (N is an integer). The simplest case is: $n = 2$ and $m = 1$ [32]. Assuming the charging time is

258   equal to the discharging time [56], one has

259      $t_{ch} = t_{dis} = t$ (32)

260   and consequently, the charging electric current equals the discharging electric current, i.e.,

261      $I_{ch} = I_{dis} = I$ (33)

262   As the regenerative efficiency is closely related to the regenerative time, the regenerative

263   efficiency of the TREC can be calculated as

264      $\eta_{RL} = \dfrac{2t_r}{\tau} = 1 - \dfrac{2m}{n}$ (34)

265   For the TREC consisting of n TREC elements, the heat absorbed from the hot reservoir and the

266   heat released to the cold reservoir can be, respectively, expressed as

267

$$Q_{2n}^* = n\left(\alpha_c T_2 C_q - I^2 R t + \frac{2m}{n}\, C_p (T_2 - T_1) \right)$$

$$= m\tau \left(\alpha_c T_2 I - I^2 R + \frac{2m}{n}\, \frac{C_p}{C_q} I (T_2 - T_1) \right)$$
        (35)

268

$$Q_{1n}^* = n\left(\alpha_c T_1 C_q + I^2 R t + \frac{2m}{n}\, C_p (T_2 - T_1) \right)$$

$$= m\tau \left(\alpha_c T_1 I + I^2 R + \frac{2m}{n}\, \frac{C_p}{C_q} I (T_2 - T_1) \right)$$
        (36)

269   Therefore, the heat fluxes in the charging and discharging processes can be, respectively,

270   calculated by

271 $$Q_{2n} = Q_{2n}^{*}/\tau = m\left(\alpha_c T_2 I - I^2 R + \frac{2m}{n}\frac{C_p}{C_q}I(T_2 - T_1)\right)$$ (37)

272 $$Q_{1n} = Q_{1n}^{*}/\tau = m\left(\alpha_c T_1 I + I^2 R + \frac{2m}{n}\frac{C_p}{C_q}I(T_2 - T_1)\right)$$ (38)

273 Hence, the power output and efficiency of the TREC can be, respectively, written as

274 $$P_T = Q_{2n} - Q_{1n}$$ (39)

275 $$\eta_T = \frac{P_T}{Q_{2n}} = \frac{Q_{2n} - Q_{1n}}{Q_{2n}}$$ (40)

276 **2.3. Photovoltaic-electrochemical hybrid system**

277 The total solar energy irradiated on the DSSC can be calculated as

278 $$Q_{ALL} = \eta_{opt}GA_D$$ (41)

279 where η_{opt} is the optical efficiency of DSSC.

280 The part of heat directly released to the environment via convection can be described as [58]

281 $$Q_L = h^{*}A_D(T - T_e)$$ (42)

282 where T_e is the environment temperature; h^{*} is the heat leak coefficient. Assuming the heat

283 transfer is governed by the forced convection from the front surface, h^{*} is taken as 2.8 W m^{-2} K^{-1}

284 [44].

285 Based on the energy conservation law, the heat transferred to the TREC can be calculated as

286 $$Q_{2n} = Q_{ALL} - P_D - Q_L$$ (43)

287 Combining Eq. (35) and Eq. (41), one may obtain the mathematical relationship between the

288 electric current density of DSSC and the electric current of the TREC

289 $$A_1 i^2 + B_1 i + C_1 = 0$$ (44)

290 where $A_1 = -mR$, $B_1 = m\alpha_c T_2 + \dfrac{2m^2 C_p(T_2 - T_1)}{nC_q}$, $C_1 = -\eta_{opt}GA_D + VJA_D - \lambda(T_2 - T_1) + h^* A_D(T_2 - T_1)$.

291   It can be seen from Eq. (44) that the bottoming TREC could deliver electricity only when the

292 following condition is fulfilled:

293 $B_1^2 - 4A_1C_1 \geq 0$ (45)

294   Based on the parameters list in Table 1 and Table 2 and Eq. (42) and Eq. (43), one may plot the

295 TREC output electric current varying with the DSSC current density, as shown in Fig. 2. It is

296 observed from Fig. 2 that the TREC electric current first decreases and then increases as the DSSC

297 current density increases. Furthermore, the TREC electric current increases with the increasing solar

298 irradiance.

299   Considering the electric power generated by the TREC, the power output and efficiency of the

300 hybrid system are, respectively, described by

301 $P = P_D + P_T$ (46)

302 $\eta = \dfrac{P_D + P_T}{Q_{ALL}}$ (47)

303 **3. Results and discussion**

304   The above mathematical model is solved by commercial software Matlab®. In this section,

305 whether the DSSC model is accurate or not will be checked, and the generic performance

306 characteristics of the hybrid system will be revealed. Moreover, parametric studies will be conducted

307 to examine how the hybrid system performance is affected by various parameters, such as porosity of

308 the electrode material, photoelectron absorption coefficient, Schottky barrier, film thickness and

309 TREC internal resistance.

3.1. Model validation

Since there is no experimental study reported on this specific hybrid system yet, the topping DSSC will be validated by comparing with both theoretical results and experimental data in the literatures. Fig. 3 (a) compares the $V \sim J$ characteristic curves between the present model and the theoretical model from Ref. [59]. It is seen that both models predict that the photovoltages are monotonic decreasing functions of current density, and $V \sim J$ curves change moderately in the middle part while change rapidly at the two ends. In addition, the photovoltage become larger as the Schottky barrier increases. However, there exists obvious discrepancy between the present model and the model in Ref. [59]. The photovoltage predicted in the present model is smaller than that predicted by the model from Ref. [59]. This is because the electron diffusion coefficient and light absorption coefficient depend on the porosity electrode material in the present model, while they are regarded as porosity-independent constants in the model in Ref. [59]. Another model validation between the present modeling results and experimental data from Ref. [62] is conducted, as shown in Fig. 3 (b). It is seen that the modeling results are in good agreement with the experimental data. It indicates that the present theoretical model could well predict the performance of an actual DSSC and the present model is more accurate than the one developed by Ni et al. [59]. Moreover, it is also found from Fig. 3 (b) that the DSSC output voltage decreases with the increasing film thickness. This is because a thicker film leads to a larger electron transport resistance, which significantly drops the DSSC output voltage.

3.2. Generic performance characteristic of the hybrid system

330 The power densities and energy efficiencies of the DSSC, TREC and hybrid system varying

331 with the DSSC operating current density is shown in Fig. 4, where $P_D^* = P_D/A_D$, $P_T^* = P_T/A_D$ and

332 $P^* = P/A_D$ are, respectively, the corresponding power densities; J_D, J_T and J_H are,

333 respectively, the operating current densities at maximum power densities $P_{D,\max}^*$, $P_{T,\max}^*$ and $P_{\max}^*$,

334 $\eta_{D,\max}$, $\eta_{T,\max}$ and $\eta_{\max}$ are maximum energy efficiencies for the DSSC, TREC and hybrid system.

335 It is found that the power output densities and energy efficiencies of the DSSC, TREC and hybrid

336 system share the same trend (i.e., first increasing and then decreasing) as the current density J

337 increases. Both power density and efficiency of the hybrid system are greater than that of the single

338 DSSC. For the parameters in Table 1 and Table 2, the maximum power density and maximum

339 efficiency for the DSSC are, respectively, 77.82 W m^{-2} and 4.94 %, and the maximum power density

340 and maximum efficiency of the hybrid system are 102.76 W m^{-2} and 6.53%, respectively. By

341 mounting a bottoming TREC, the power density and efficiency of the DSSC are improved by

342 32.04% and 32.18% compared with the sole DSSC, respectively. It clearly shows that the proposed

343 method in this paper is feasible and effective, and the TREC can be treated as a potential waste heat

344 recovery candidate for DSSC.

345 **3.3. Effect of the electrode porosity**

346 The porosity of the electrode has a decisive influence on the light absorption coefficient and

347 electron diffusion coefficient of the DSSC [63], and therefore, the porosity greatly affects the overall

348 hybrid system performance.

349 Based on both experimental and modeling results [64], the effects of electrode porosity on the

350 light absorption coefficient [65] and the electron diffusion coefficient can be expressed as [66]

351 $$\alpha = 2586\left(1-\varepsilon\right)\left(\varepsilon + 2.89\right) \tag{48}$$

352 $$D = a\left|\varepsilon - \varepsilon_c\right|^{\mu} \qquad \varepsilon \leq 0.41 \tag{49}$$

353 $$\alpha = 2.97 \times 10^4 \varepsilon^2 \tag{50}$$

354 $$D = 1.69 \times 10^{-4}\left(-14.78\varepsilon^3 + 7.39\varepsilon^2 - 2.89\varepsilon + 2.15\right) \qquad \varepsilon \geq 0.41 \tag{51}$$

355 where ε is porosity of DSSC electrode material, a , μ and the critical porosity ε_c are 4×10^{-4}

356 $cm^2 s^{-1}$, 0.82 and 0.76, respectively [25].

357   As shown in Fig. 5 (a), the light absorption coefficient and electron diffusion coefficient display

358 different features in the whole range of electrode porosity. The electron diffusion coefficient

359 approximately decreases from $3.58\times10^{-4}\,m^2\,s^{-1}$ to $5.89\times10^{-5}\,m^2\,s^{-1}$ as the electrode porosity increases

360 from 0 to 0.41. The electron diffusion coefficient first decreases from $2.54\times10^{-4}\,m^2\,s^{-1}$ to 0 when the

361 porosity increases from 0.41 to 0.76, and then it grows to $1.86\times10^{-4}\,m^2\,s^{-1}$ as the electrode porosity

362 approaches 1.0. The light absorption coefficient first grows and then decreases as the electrode

363 porosity increases, and its maximum value is about $5000\,cm^{-1}$ when the porosity is 0.41.

364   It is well-known that the short-circuit current density of DSSC is a key factor affecting the

365 DSSC performance and thus the hybrid system performance. As shown in Fig. 5 (b), the short-circuit

366 current density increases to attain its maximum $7.81\,A\,m^{-2}$ and then begins to drop as the electrode

367 porosity increases. As the electrode porosity gradually increases, the ability of the electrode material

368 to absorb photoelectrons gradually increases while the electron diffusion coefficient gradually

369 decreases. Therefore, the compound effect is that the number of electrons entering the circulation

370 state gradually increases. However, when the electrode porosity continues to increase, the mass of

371 the TiO_2 film per unit area will decrease, so the surface area of the TiO_2 film per unit area decreases

372   and the number of dye molecules adsorbed by the thin film per unit area become less. Finally, the

373   current density of the short-circuit eventually decreases with the increase of electrode porosity.

374   **3.4. Effect of the photoelectron absorption coefficient**

375   The $\eta \sim J$ curves for different photoelectron absorption coefficients [66] are shown in Fig. 6. It

376   is seen that both efficiency and power output density of the hybrid system increase with an increase

377   in the photoelectron absorption coefficient, and the current density corresponding to the maximum

378   efficiency or maximum power density also shifts rightward with the increasing photoelectron

379   absorption coefficient. Meanwhile, the limiting current density for either efficiency or power density

380   of the hybrid system is enlarged as the photoelectron absorption coefficient increases. It should be

381   noted that both efficiency and power density are less sensitive to the change of photoelectron

382   absorption coefficient when the photoelectron absorption coefficient exceeds 5.0×10^5 m^{-1}. This is

383   because the power output of the hybrid system first sharply and then slowly increases as the

384   photoelectron absorption coefficient increases to 5.0×10^5 m^{-1}, as shown in Fig. 6 (c). As the

385   photoelectron absorption coefficient increases from 5.0×10^5 m^{-1}, the power density of the hybrid

386   system is almost unchanged. Hence, an appropriate photoelectron absorption coefficient should be

387   carefully selected since high photoelectron absorption coefficient may tremendously increase the

388   manufacture cost for DSSCs.

389   **3.5. Effect of the Schottky barrier**

390   As shown by Eq. (1), the Schottky barrier of combination interface has a significant impact on

391   the voltage loss. With the help of the Schottky barrier model [58], the voltage loss V_1 varying with

392   the Schottky barrier Φ_b can be obtained, as shown in Fig. 7 (a). The voltage loss maintains

393 negligibly small when the Schottky barrier is smaller than 0.5 eV. As the Schottky barrier increases

394 from 0.5 eV, the voltage loss sharply increases. The effects of the operating temperature on the

395 voltage loss are negligible when the Schottky barrier is below 0.5 eV and becoming obvious with a

396 further increase in the Schottky barrier. In addition, the voltage loss decreases as the DSSC operating

397 temperature is elevated. This is because it is easier for the electrons at higher temperature to

398 crossover the combination interface [67] with a smaller voltage loss. Therefore, the performance of

399 DSSC can be optimized by adjusting the Schottky barrier to reduce the voltage loss at the composite

400 interface [68].

401 Fig. 7 (b) shows that both efficiency and power output of the DSSC are almost unchanged when

402 the Schottky barrier is below 0.5 eV and improved as the operating temperature increases due to the

403 reduced voltage losses. Fig. 7 (c) and Fig. 7 (d) show that the efficiency and power output of the

404 hybrid system varying with the operating current density for different Schottky barriers. It is seen

405 that both efficiency and power output of the hybrid system are improved as the Schottky barrier is

406 reduced, and the current densities corresponding to the maximum power density and maximum

407 efficiency are also enlarged. However, the effects of Schottky barrier on the hybrid system

408 performance become insensitive as the Schottky barrier is smaller than 0.5 eV.

409 **3.6. Effect of the film thickness**

410 A larger film thickness means it incorporates more dye molecules to produce electrons, and thus

411 the photoelectron current density will be increased [69]. When the film thickness exceeds a certain

412 length and continues to grow, the transport distance of the produced electrons will be also

413 simultaneously increased, which in return drops the photoelectron current density. Fig. 8 shows the

414   effects of film thickness on the efficiency and power density of the hybrid system. Both efficiency

415   and power density of the hybrid system first increase and then decrease as the film thickness is

416   increased. The limiting current density for the hybrid system is also first increased and then

417   decreased with an increase in the film thickness. For the parameters given in Table 1 and Table 2, the

418   optimum film thickness is found to be between 1.0×10^{-2} and 4.0×10^{-2} mm.

419   **3.7. Effect of the internal resistance of thermally regenerative electrochemical cycle**

420   The TREC internal resistance is an important factor affecting the performance of TREC and

421   thus affecting the overall hybrid system performance as well. As shown in Fig. 9, both efficiency and

422   power density of the hybrid system are improved as the TREC internal resistance is reduced. This is

423   because a smaller TREC internal resistance indicates that less heat is wasted per unit time in the

424   TREC. It is also seen from Fig. 9 that the working current density range of TREC becomes narrower

425   as the TREC internal resistance increases. Fig. 9 (c) further shows that the maximum power density

426   and maximum efficiency of the hybrid system continuously decline as the TREC internal resistance

427   increases. Therefore, reducing the TREC internal resistance is an important mean to effectively

428   improve the hybrid system performance.

429   **4. Conclusions**

430   A novel photovoltaic-electrochemical hybrid system composed of a DSSC, an SSA and a TREC

431   is proposed with the aim to harvest the relatively high wavelength sunlight that not utilized by the

432   DSSC. The models of DSSC and TREC are mathematically described in detail, and the condition

433   that the bottoming TREC participates in the additional electricity generation is derived. The DSSC

434   model is demonstrated to be accurate by comparing with both modeling results and experimental

435 data in the current literatures. It is feasible and effective to use TREC as an alternative waste heat

436 recovery technology for DSSC. Through mounting a bottoming TREC, the maximum power density

437 and maximum efficiency of the hybrid system gain increases by 32.04% and 32.18% in comparison

438 with the single DSSC, respectively. Extensive parametric studies are carried out to examine how the

439 hybrid system performance is impacted by some microstructure parameters and operating conditions.

440 The light absorption coefficient, electron diffusion coefficient and short-circuit current density

441 display different trends varying with the electrode porosity. An increase in photoelectron absorption

442 coefficient improves the efficiency and power output density of the hybrid system, while an increase

443 in Schottky barrier or internal resistance of TREC degrades the hybrid system performance. It is also

444 found that there exists an optimum film thickness to maximize the efficiency and power output

445 density of the hybrid system. The obtained results offer some new insights into further improving the

446 performance of photovoltaic cells through hybridizing feasible TRECs.

447

Nomenclature

448	**Nomenclature**	
449	A	Active area (m^2)
450	A^*	Richardson constant (A m^{-2} K^{-2})
451	C_p	Heat capacity (J kg^{-1} K^{-1})
452	C_q	Charge capacity (A s^{-1} kg^{-1})
453	d	Thickness of the thin film (m)
454	D	Electron diffusion coefficient (m^2 s^{-1})
455	G	Solar spectrum intensity (W m^{-2})
456	h	Planck constant (J s^{-1})
457	h^*	Heat leak coefficient (W m^{-2} K^{-1})
458	I	Current of TREC (A)
459	J	Current density of the DSSC (A m^{-2})
460	k	Boltzmann constant (J K^{-1})
461	L	Electron diffusion length (m)
462	m^*	Equal to 5.6 times the electron mass (g)
463	$m^{\#}$	Ideality factor
464	m	Number of the cells charged simultaneously
465	n	Number of TREC
466	$n(x)$	Excessive electron concentration (cm^{-3})
467	n_0	Electron concentration under a dark condition (cm^{-3})
468	P	Power output (W)

469	P^*	Power output density (W m^{-2})
470	Q	Heats for a TREC (J)
471	Q^*	Heats for a TREC (J)
472	q	Electron charge (C)
473	q^*	Heats (J)
474	R	Electric resistance (Ω)
475	T	Operating temperature (K)
476	t	Time (s)
477	V_0	Potential difference of the redox potential (V)
478	V_1	Voltage loss at the TiO_2/TCO interface (V)

479 **Greek symbols**

480	Φ	Light intensity ($\text{m}^{-2}\,\text{s}^{-1}$)
481	Φ_0	Light intensity at 1 sun condition ($\text{m}^{-2}\,\text{s}^{-1}$)
482	Φ_b	Schottky barrier height (eV)
483	τ	Cycle time (s)
484	τ^*	Electron lifetime (s)
485	η	Efficiency
486	λ	Decreasing rate of the power output density (W K^{-1})
487	β	Decreasing rate of efficiency (K^{-1})
488	α_c	Temperature coefficient (V K^{-1})
489	α	Light absorption coefficient of the electrode (m^{-1})

490 **Superscripts and subscripts**

491 1   Cold source

492 2   Heat source

493 All   Gross

494 D   DSSC

495 e   Environment

496 T   TREC

497 L   Heat release

498 dev   Deviations

499 RL   Regenerative losses

500 ref   Reference

501 opt   Optimal state

502 r   Recombination process

503 dis   Discharge process

504 ch   Charge process

505 n   Number of TREC

506 J   Joule

507 sc   Short-circuit current density

508

514

515

References

[1] Liu J. China's renewable energy law and policy: A critical review. Ren Sust Energy Rev 2019; 99: 212-9.

[2] Ju X, Xu C, Hu Y, Han X, Wei G, Du X. A review on the development of photovoltaic/concentrated solar power (PV-CSP) hybrid systems. Sol Energy Mat Sol Cells 2017; 161: 305-27.

[3] Husain AAF, Hasan WZW, Shafie S, Hamidon MN, Pandey SS. A review of transparent solar photovoltaic technologies. Ren Sust Energy Rev 2018; 94: 779-91.

[4] Mathew S, Yella A, Gao P, Humphry-Baker R, Curchod BFE, Ashari-Astani N, et al. Dye-sensitized solar cells with 13% efficiency achieved through molecular engineering of porphyrin sensitizers. Nat Chem 2014; 6: 242-7.

[5] Ye M, Wen X, Wang M, Ioozzia J, Zhang N, Lin C, et al. Recent advances in dye-sensitized solar cells: from photoanodes, sensitizers, and electrolytes to counter electrodes. Mat Today 2015; 18: 155-62.

[6] Pounraj P., Mohankumar V., Pandian MS, and Ramasamy P. Anthocyanin modified triphenylamine based organic sensitizer for dye sensitized solar cells (DSSC) - A theoretical approach. AIP Conf Proc 2017; 1832: 090037.

[7] Sengupta D, Das P, Mondal B, Mukherjee K. Effects of doping, morphology and film-thickness of photo-anode materials for dye sensitized solar cell application – A review. Ren Sust Energy Rev 2016; 60: 356-76.

[8] Chen X, Tang Q, He B, Lin L, Yu L. Platinum-free binary Co-Ni alloy counter electrodes for efficient dye-sensitized solar cells. Ang chem Int Ed 2014; 53: 10799-803.

[9] Huen P, Daoud WA. Advances in hybrid solar photovoltaic and thermoelectric generators. Ren Sust Energy Rev 2017; 72: 1295-302.

[10] Su S, Chen X, Wang J, Chen J. Performance evaluation and parametric optimum design of a thermoelectric refrigerator driven by a dye-sensitized solar cell. Int J Refrig 2015; 60: 62-9.

[11] Pounraj P., Prince Winston D., Kabeel A.E., Praveen Kumar B., Muthu Manokar A., Sathyamurthy R, Cynthia Christabel S. Experimental investigation on Peltier based hybrid PV/T

active solar still for enhancing the overall performance. Energy Convers Managem 2018; 168: 371–81.

[12] Praveen kumar B., Prince Winston D., Pounraj P., Muthu Manokar A., Sathyamurthy R, Kabeel A.E. Experimental investigation on hybrid PV/T active solar still with effective heating and cover cooling method. Desalination 2018; 435: 140–51.

[13] Mahmoudinezhad S, Rezaniakolaei A, Rosendahl LA. Numerical parametric study on the performance of CPV-TEG hybrid system. Energy Procedia 2019; 158: 453–8.

[14] Li F, Shittu S, Thierno M.O.D, Yu M, Zhao X, Ji J. A review of solar photovoltaic-thermoelectric hybrid system for electricity generation. Energy 2018; 158: 41-58.

[15] Babu C, Ponnambalam P. The theoretical performance evaluation of hybrid PV-TEG system. Energy Convers Managem 2018; 173: 450–60.

[16] Wang N, Han L, He H, Park NH, Koumoto K. A novel high-performance photovoltaic-thermoelectric hybrid device. Energy Environ Sci 2011; 4: 3676-79.

[17] Xu L, Xiong Y, Mei A, Hu Y, Rong Y, Zhou Y, et al. Efficient perovskite photovoltaic-thermoelectric hybrid device. Adv Energy Mat 2018; 8: 1702937.

[18] Kil TH, Kim S, Jeong DH, Geum DM, Lee S, Jung SJ, et al. A highly-efficient, concentrating-photovoltaic/thermoelectric hybrid generator. Nano Energy 2017; 37: 242-7.

[19] Yin E, Li Q, Xuan Y. Optimal design method for concentrating photovoltaic-thermoelectric hybrid system. Appl Energy 2018; 226: 320-9.

[20] Yin E, Li Q, Xuan Y. Feasibility analysis of a concentrating photovoltaic-thermoelectric-thermal cogeneration. Appl Energy 2019; 236: 560-73.

[21] Mahmoudinezhad S, Rezania A, Rosendahl LA. Bahavior of hybrid concentrated photovoltaic-thermoelectric generator under variable solar radiation. Energy Convers Managem 2018; 164: 443-52.

[22] Park WT, Shin SM, Tazebay AS, Um HD, Jung JY, JeeSW, et al. Lossless hybridization between photovoltaic and thermoelectric devices. Sci Rep 2013; 3: 2123.

[23] Bjørk R, Nielsen KK. The maximum theoretical performance of unconcentrated solar photovoltaic and thermoelectric generator systems. Energy Convers Managem 2018; 156: 264-8.

572 [24] Yang Y, Lee SW, Ghasemi H, Loomis J, Li X, Kraemer D, et al. Charging free electrochemical

573 system for harvesting low-grade thermal energy. Proc Nation Acad Sci USA 2014; 111: 17011-16.

574 [25] Lee SW, Yang Y, Lee HW, Ghasemi H, Kraemer D, Chen G, et al. An electrochemical system

575 for efficiently harvesting low-grade heat energy. Nat Commun 2014; 5: 3942.

576 [26] Gao C, Lee SW, Yang Y. Thermally regenerative electrochemical cycle for low-grade heat

577 harvesting. ACS Energy Lett 2017; 2: 2326-34.

578 [27] Zhang F, Liu J, Yang W, Logan BE. A thermally regenerative ammonia-based battery for

579 efficient harvesting of low-grade thermal energy as electrical power. Energy Environ Sci 2015; 8:

580 343-9.

581 [28] Ling R, Li B, Liu Z, Liu W. Performance analysis of a dual loop thermally regenerative

582 electrochemical cycle for waste heat recovery. Energy 2016; 107: 388-95.

583 [29] Long R, Li B, Liu Z, Liu W. Performance analysis of a thermally regenerative electrochemical

584 cycle for harvesting waste heat. Energy 2015; 87: 463-9.

585 [30] Long R, Li B, Liu Z, Liu W. Ecological analysis of a thermally regenerative electrochemical

586 cycle. Energy 2016; 107: 95-102.

587 [31] Long R, Li B, Liu Z, Liu W. Multi-objective optimization of a continuous thermally

588 regenerative electrochemical cycle for waste heat recovery. Energy 2015; 93: 1022-9.

589 [32] Wang Y, Cai L, Peng W, Zhou Y, Chen J. Maximal continuous power output and parametric

590 optimum design of an electrochemical system driven by low-grade heat. Energy Convers Managem

591 2017; 138: 156-61.

592 [33] Guo J, Wang Y, Gonzalez-Ayala J, Roco JMM, Medina A, Calvo Hernández A. Continuous

593 power output criteria and optimum operation strategies of an upgraded thermally regenerative

594 electrochemical cycles system. Energy Convers Managem 2019; 180: 654-64.

595 [34] Yang Y, Lee SW, Ghasemi H, Loomis J, Li X, Kraemer D, Zheng G, Cui Y, and Chen G.

596 Charging-free electrochemical system for harvesting low-grade thermal energy. PNAS 2014; 48:

597 17011–16.

598 [35] Yang Y, Loomis J, Ghasemi H, Lee SW, Wang YJ, Cui Y and Chen G. Membrane-free battery

599 for harvesting low-grade thermal energy. Nano Lett 2014; 14: 6578−83.

600   [36] Long R, Li B, Liu Z, Liu W. A hybrid system using a regenerative eletrochemical cycle to

601   harvest waste heat from the proton exchange membrane fuel cell. Energy 2015; 93: 2079-86.

602   [37] Zhang X, Pan Y, Cai L, Zhao Y, Chen J. Using electrochemical cycles to efficiently exploit the

603   waste heat from a proton exchange membrane fuel cell. Energy Convers Managem 2017; 144:

604   217-23.

605   [38] Zhang X, Cai L, Liao T, Zhou Y, Zhao Y, Chen J. Exploiting the waste heat from an alkaline

606   fuel cell via electrochemical cycles. Energy 2018; 142: 983-90.

607   [39] Wang N, Han L, He H, Park NH and Koumoto K. A novel high-performance

608   photovoltaic–thermoelectric hybrid device. Energy Environ Sci 2011; 4: 3676.

609   [40] Liu SH, Fu H, Cheng YM, Wu KL, Ho ST, Chi Y and Chou PT. Theoretical study of N749 dyes

610   anchoring on the (TiO_2) 28 surface in DSSCs and their electronic absorption properties. J Phys Chem

611   C 2012; 116: 16338−45.

612   [41] Dürr M., Bamedi A., Yasuda A. and Nelles G. Tandem dye-sensitized solar cell for improved

613   power conversion efficiencies. Appl Phys Lett 2004; 84: 3397.

614   [42] Selvakumar N., Krupanidhi S. B. and Barshilia HC. Carbon nanotube-based tandem absorber

615   with tunable spectral selectivity: transition from near-perfect blackbody absorber to solar selective

616   absorber. Adv Mat 2014; 26: 2552–7.

617   [43] Guo XZ, Zhang YD, Qin D, Luo YH, Li DM, Pang YT and Meng QB. Hybrid tandem solar cell

618   for concurrently converting light and heat energy with utilization of full solar spectrum. J Power

619   Sources 2010; 195: 7684–90.

620   [44] Su S, Liu T, Wang Y, Chen X, Wang J, Chen J. Performance optimization analyses and

621   parametric design criteria of a dye-sensitized solar cell thermoelectric hybrid device. Appl Energy

622   2014; 120: 16-22.

623   [45] Ayalew WA, Ayele DW. Dye-sensitized solar cells using natural dye as light-harvesting

624   materials extracted from Acanthus sennii chiovenda flower and Euphorbia cotinifolia leaf. J Sci: Adv

625   Mat Dev 2016; 1: 488-94.

626   [46] Narayan MR. Review: Dye sensitized solar cells based on natural photosensitizers. Renew Sust

627   Energy Rev 2012; 16: 208-15.

628 [47] Sodergren S, Hagfeldt A, Olsson J, Lindquist SE. Theoretical Models for the Action Spectrum

629 and the Current-Voltage Characteristics of Microporous Semiconductor Films in

630 Photoelectrochemical Cells. J Phys Chem 1994; 98: 5552-56.

631 [48] McConnell RD. Assessment of the dye-sensitized solar cell. Renew Sust Energy Rev 2002; 6:

632 273-95.

633 [49] Gomez R, Salvador P. Photovoltage dependence on film thickness and type of illumination in

634 nanoporous thin film electrodes according to a simple diffusion model. Sol Energy Mat Solar Cells

635 2005; 88: 377–88.

636 [50] Gratzel M. Solar Energy Conversion by Dye-Sensitized Photovoltaic Cells. Inorg. Chem. 2005;

637 44: 6841-51.

638 [51] Berginc M, Krasovec UO, Janvokec M, Topic M. The effect of temperature on the performance

639 of dye-sensitized solar cells based on a propyl-methyl-imidazolium iodide electrolyte. Sol Energy

640 Mat Solar Cells 2007; 91: 821-28.

641 [52] Zhang W, Zhu R, Liu B, Ramakrishna S. High-performance hybrid solar cells employing

642 metal-free organic dye modified TiO_2 as photoelectrode. Appl Energy 2012; 90: 305-8.

643 [53] Sebastian PJ, Olea A, Campos J, Toledo JA, Gamboa SA. Temperature dependence and the

644 oscillatory behavior of the opto-electronic properties of a dye-sensitized nanocrystalline TiO_2 solar.

645 Sol Energy Mat Solar Cells 2004; 81: 349-61.

646 [54] Wang Y, Li H, Hao H, Chen X. Performance optimization of a photovoltaic solar cell-based

647 hybrid system. J Renew Sust Energy 2018; 10: 044702.

648 [55] Zhang J, Xuan Y, Yang L. A novel choice for the photovoltaic-thermoelectric hybrid system:

649 the perovskite solar cell. Int J Energy Res 2016; 40: 1400-09.

650 [56] Long R, Li B, Liu Z, Liu W. Performance analysis of a dual loop thermally regenerative

651 electrochemical cycle for waste heat recovery. Energy 2016; 107: 388-95.

652 [57] Ni M, Leung MKH, Leung DYC, Sumathy K. An analytical study of the porosity effect on

653 dye-sensitized solar cell performance. Sol Energy Mat Solar Cells 2006; 90: 1331-44.

654 [58] Chow TT, He W, Ji J. Hybrid photovoltaic-thermosyphon water heating system for residential

655 application. Solar Energy 2006; 80: 298-306.

656 [59] Ni M, Leung MKH, Leung DYC, Sumathy K. Theoretical modeling of TiO_2/TCO interfacial

657 effect on dye-sensitized solar cell performance. Sol Energy Mat Solar Cells 2006; 90: 2000-9.

658 [60] Gomez R, Salvador P. Photovoltage dependence on film thickness and type of illumination in
659 nanoporous thin film electrodes according to a simple diffusion model. Sol Energy Mat Solar Cells
660 2005; 88: 377-88.

661 [61] Ferber J, Luther J. Modeling of photovoltage and photocurrent in dye-sensitized titanium
662 dioxide solar cells. J Phys Chem B 2001; 105: 4895-903.

663 [62] Ni M, Leung MKH, Leung DYC. Theoretical modeling of the electrode thickness effect on
664 maximum power point of dye-sensitized solar cell. Can J Chem Eng 2008; 86: 35-42.

665 [63] Benkstein KD, Kopidakis N, Lagemaat J, Frank AJ. Influence of the Percolation Network
666 Geometry on Electron Transport in Dye-Sensitized Titanium Dioxide Solar Cells. J Phys Chem B
667 2003; 107: 7759-67.

668 [64] Rothenberger G, Comte P, Gratzel M. A contribution to the optical design of dye-sensitized
669 nanocrystalline solar cells. Sol Energy Mat Solar Cells 1999; 58: 321-36.

670 [65] Fredin K, Nissfolk J, Hagfeldt A. Brownian dynamics simulations of electrons and ions in
671 mesoporous films. Sol Energy Mat Solar Cells 2005; 86: 283-97.

672 [66] Lee JJ, Coia GM, Lewi NS. Current Density versus Potential Characteristics of Dye-Sensitized
673 Nanostructured Semiconductor Photoelectrodes.1. Analytical Expressions. J Phys Chem B 2004; 108:
674 5269-81.

675 [67] Tang J, White M, Stucky GD, McFarland EW, Electrochemical fabrication of large-area
676 Au/TiO$_2$ junctions. Electrochem Commun 2003; 5: 497-501.

677 [68] Kron G, Rau U, Werner JH. Influence of the Built-in Voltage on the Fill Factor of
678 Dye-Sensitized Solar Cells. J Phys Chem B 2003; 107: 13258-61.

679 [69] Hara K, Horiguchi T, Kinoshita T, Sayama K, Sugihara H, Arakawa H. Highly efficient
680 photon-to-electron conversion with mercurochrome-sensitized nanoporous oxide semiconductor
681 solar cells. Sol Energy Mat Solar Cells 2000; 64: 115-34.

682

683 **Table captions:**

684

685 Table 1. Parameters used in the DSSC modeling.

686 Table 2. Parameters used in the TREC modeling.

687

688 **Figure captions:**

689

690 Fig. 1. Conceptual diagram of the photovoltaic-electrochemical hybrid system.

691 Fig. 2. TREC output electric current varying with the DSSC current density.

692 Fig. 3. Comparisons between the present modeling results and (a) the modeling results from Ref.

693 [59], where $m^{\#}$ equals 4.5; and (b) the experimental data from Ref. [62].

694 Fig. 4. (a) Efficiency and (b) power density comparisons between the DSSC, TREC and hybrid

695 system, where J_D, J_T and J_H are, respectively, the operating current densities at maximum

696 power densities $P^*_{D,\max}$, $P^*_{T,\max}$ and $P^*_{\max}$; $\eta_{D,\max}$, $\eta_{T,\max}$ and $\eta_{\max}$ are maximum energy

697 efficiencies for the DSSC, TREC and hybrid system.

698 Fig. 5. (a) electron diffusion coefficient and light absorption coefficient and (b) short-circuit current

699 density varying with the electrode porosity.

700 Fig. 6. Effects of the photoelectron absorption coefficient on (a) $\eta \sim J$, (b) $P^* \sim J$ and (c) P^*.

701 Fig. 7. Effects of the Schottky barrier on (a) voltage loss, (b) power density and efficiency of DSSC,

702 (c) efficiency of the hybrid system, and (d) power density of the hybrid system.

703 Fig. 8. Effects of the film thickness on (a) efficiency and (b) power density of the hybrid system.

704   Fig. 9. Effects of the TREC internal resistance on (a) efficiency, (b) power density, and (c) maximum

705   power density and maximum efficiency of the hybrid system.

706

707 **Table 1.** Parameters used in the DSSC modeling.

Parameters	Value
n_0 (m^{-3})	1.0×10^{22}
Φ_0 (m^{-2} s^{-1})	1.0×10^{21}
Φ_b (J) [59]	1.12×10^{-19}
α (m^{-1}) [60]	5.0×10^{5}
D (m^2 s^{-1}) [60]	2.0×10^{-8}
τ (s)	10×10^{-2}
A^* (A m^{-2} K^{-2}) [60]	6.71×10^{6}
d (m) [60]	10×10^{-6}
T (K)	330
T_{ref} (K)	298
T_e (K)	298
q (C)	1.60218×10^{-19}
k	1.38006×10^{-23}
G (W m^{-2}) [61]	1000
h	6.626×10^{-34}
η_{opt} [53]	0.970
h^* (W m^{-2} K^{-1}) [53]	2.8
λ (W K^{-1}) [53]	0.00506×10^{-3}
β (K^{-1})	0.0114
$m^\#$ [62]	4.5

709
710
711
712
713
714
715
716
717
718
719
720
721
722
723
724
725
726
727
728
729

730   **Table 2.** Parameters used in the TREC modeling.

731

Parameters	Value
R (Ω)	0.004
α_c (V K^{-1})	0.027
m [32]	1.0
n [32]	2.0
T_2 (K)	330
T_1 (K)	298
C_p (J kg^{-1}K^{-1}) [32]	2.408
C_q (A h kg^{-1}) [32]	32.43

741

742

743

744   Fig. 1.
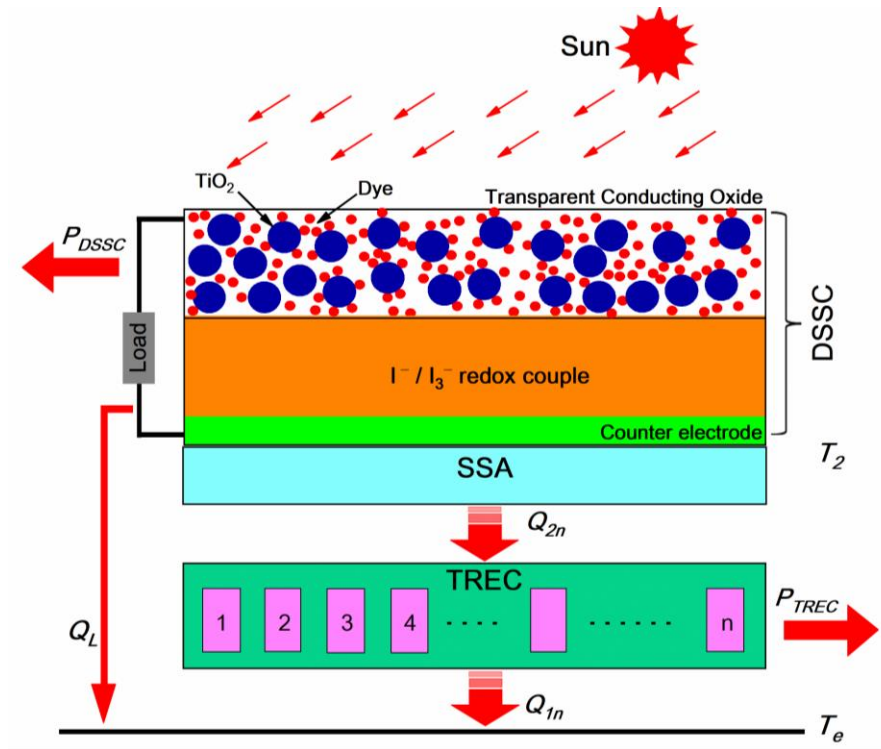
Fig. 1. Conceptual diagram of the photovoltaic-electrochemical hybrid system.

745

746

747

748   Fig. 2.
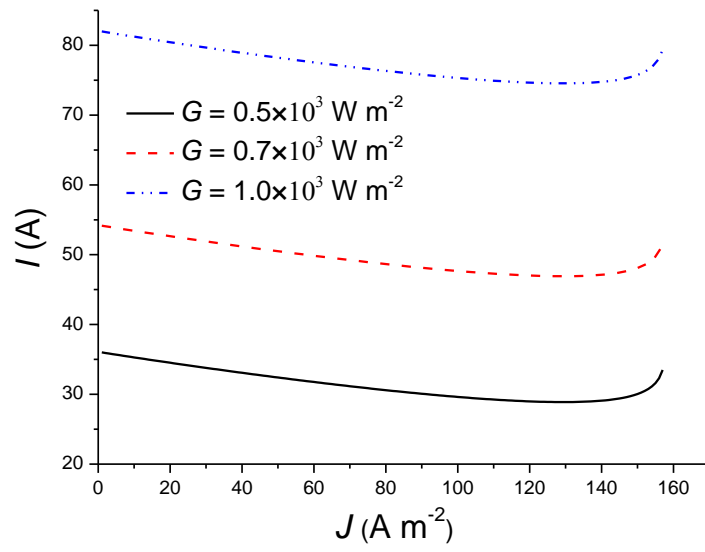
749

750   Fig. 2. TREC output electric current varying with the DSSC current density.

751

752 Fig. 3.

(a)

753

754

(b)

755

756 Fig. 3. Comparisons between the present modeling results and (a) the modeling results from Ref.

757 [59], where $m^{\#}$ equals 4.5; and (b) the experimental data from Ref. [62].

758

759   Fig. 4.

(a)

760

761

(b)
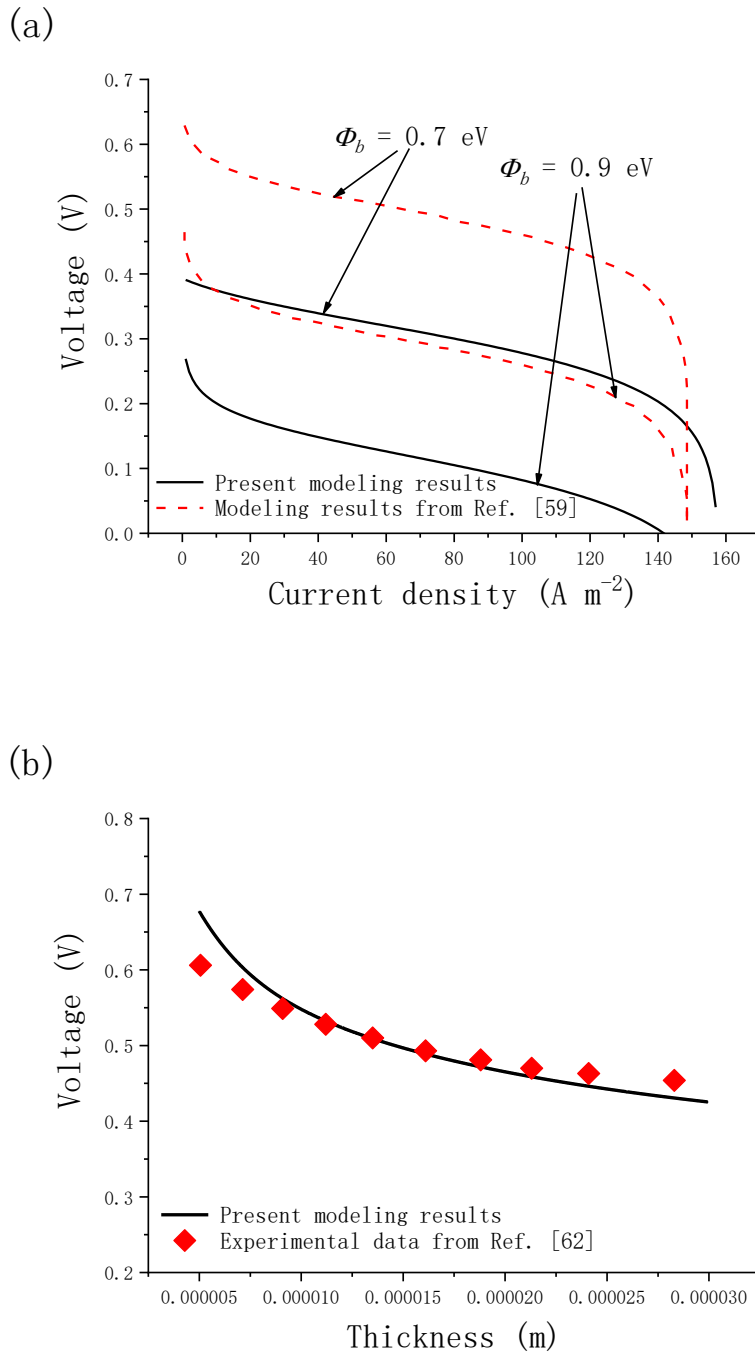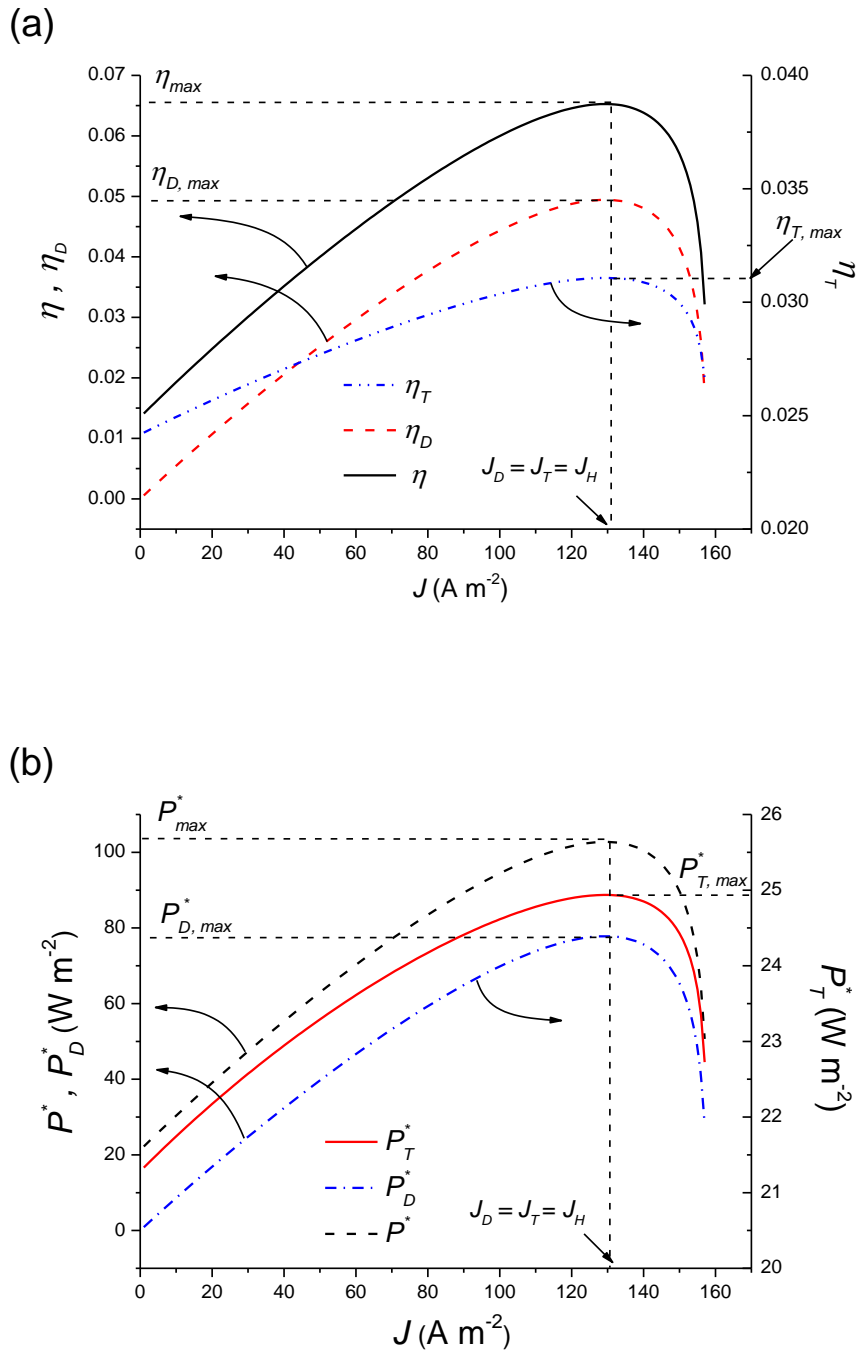
762

763   Fig. 4. (a) Efficiency and (b) power density comparisons between the DSSC, TREC and hybrid

764   system, where J_D, J_T and J_H are, respectively, the operating current densities at maximum

765   power densities $P_{D,max}^*$, $P_{T,max}^*$ and P_{max}^*; $\eta_{D,max}$, $\eta_{T,max}$ and η_{max} are maximum energy

766   efficiencies for the DSSC, TREC and hybrid system.

767   41

768   Fig. 5.

(a)

769

(b)
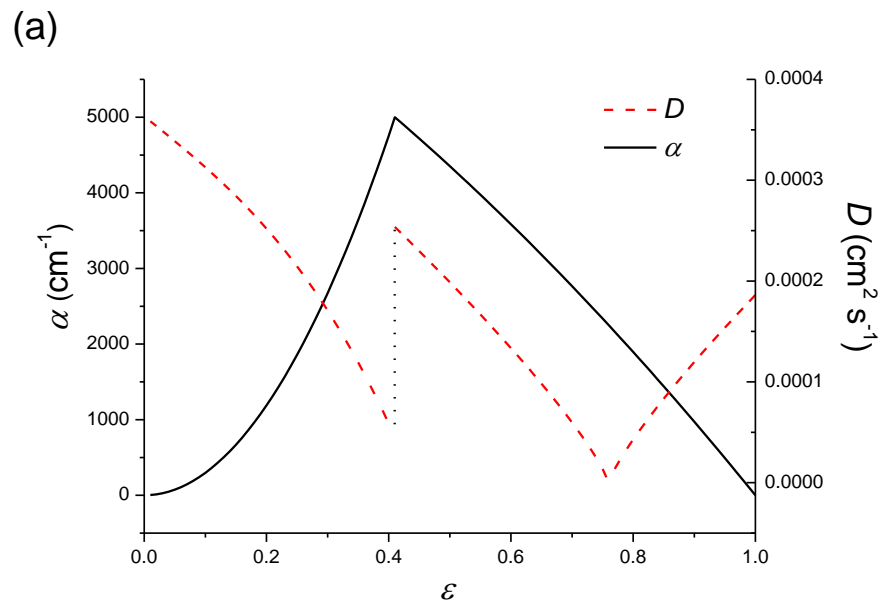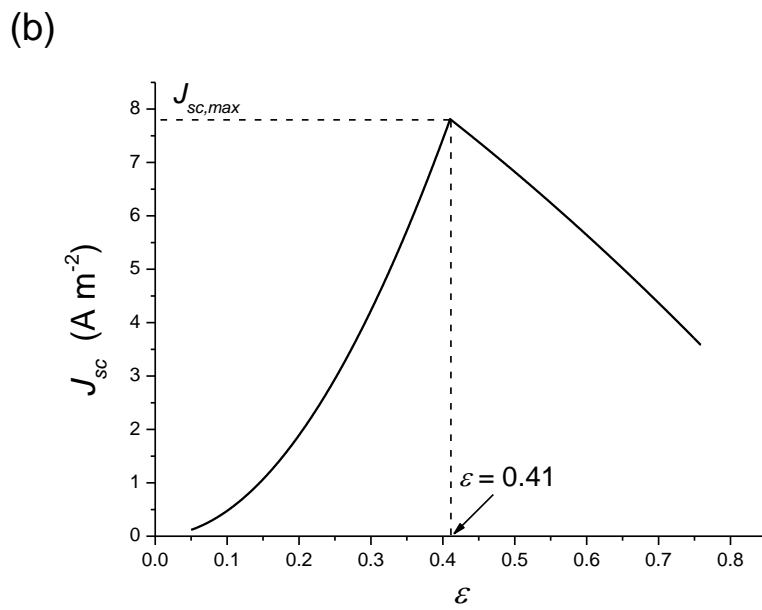
770

771   Fig. 5. (a) electron diffusion coefficient and light absorption coefficient and (b) short-circuit current

772   density varying with the electrode porosity.

773

774   Fig. 6.

(a)

775

776

(b)

777

(c)
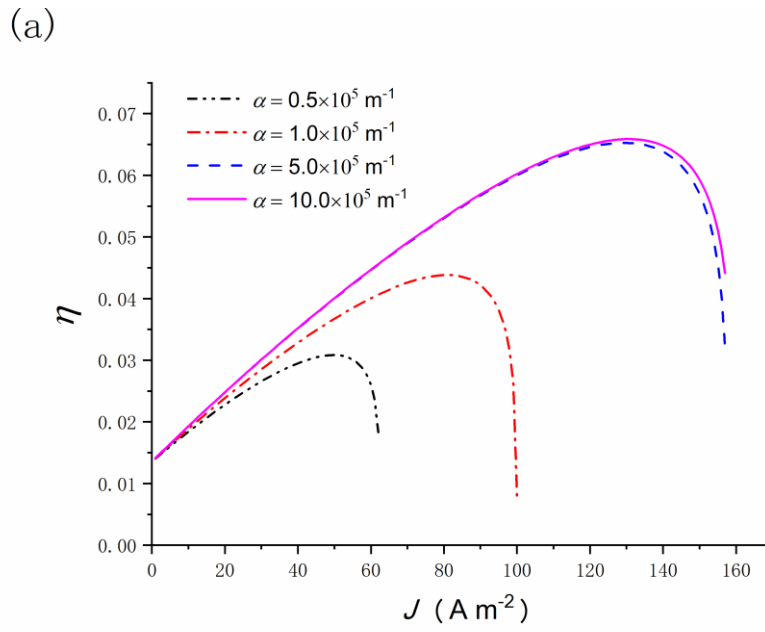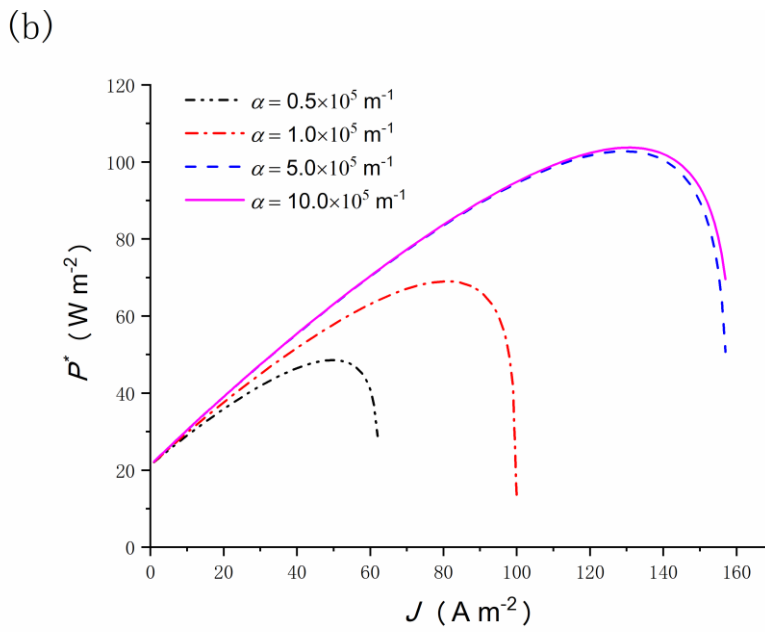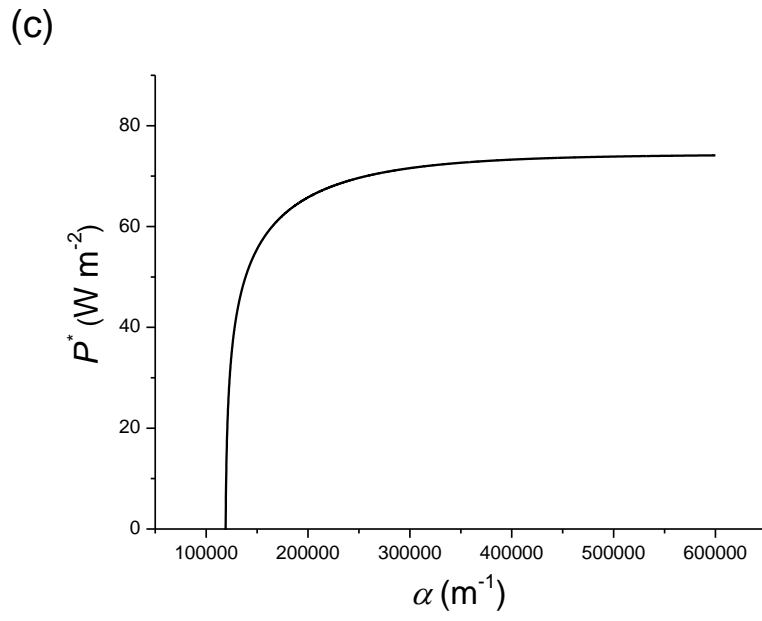
778

779   Fig. 6. Effects of the photoelectron absorption coefficient on (a) $\eta \sim J$, (b) $P^* \sim J$ and (c) P^* .
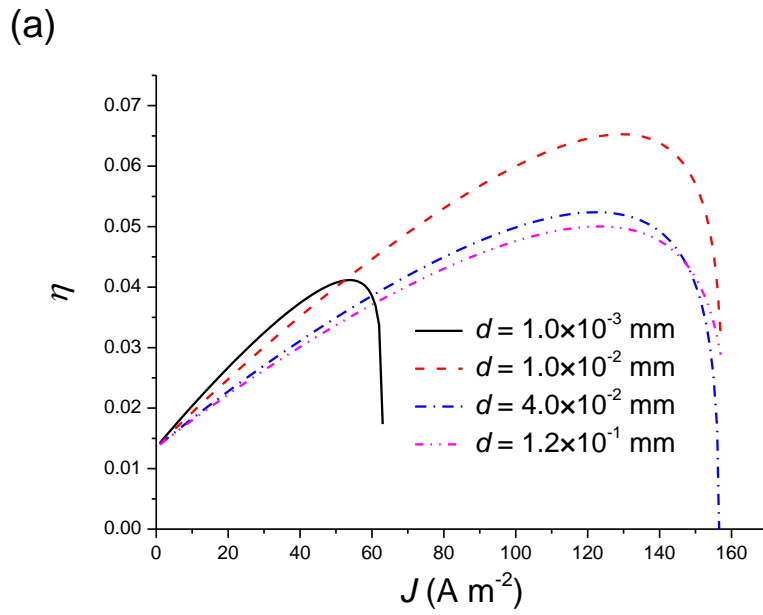
780

781   Fig. 7.

(a)

782

(b)

783

784

(c)

785

(d)
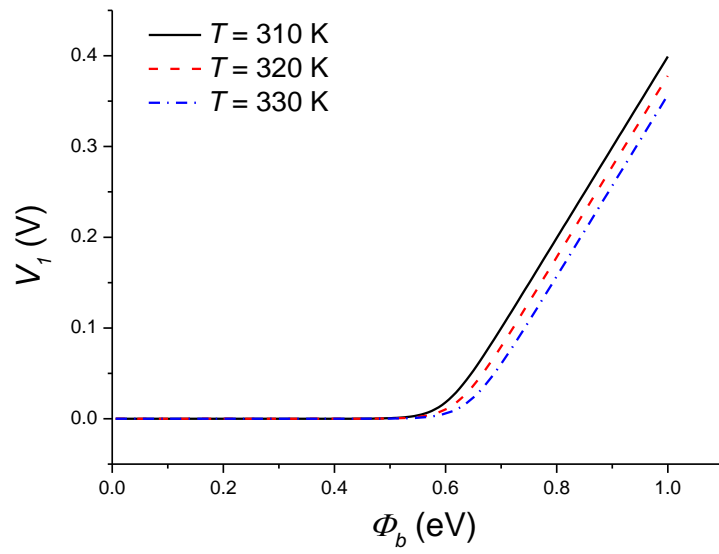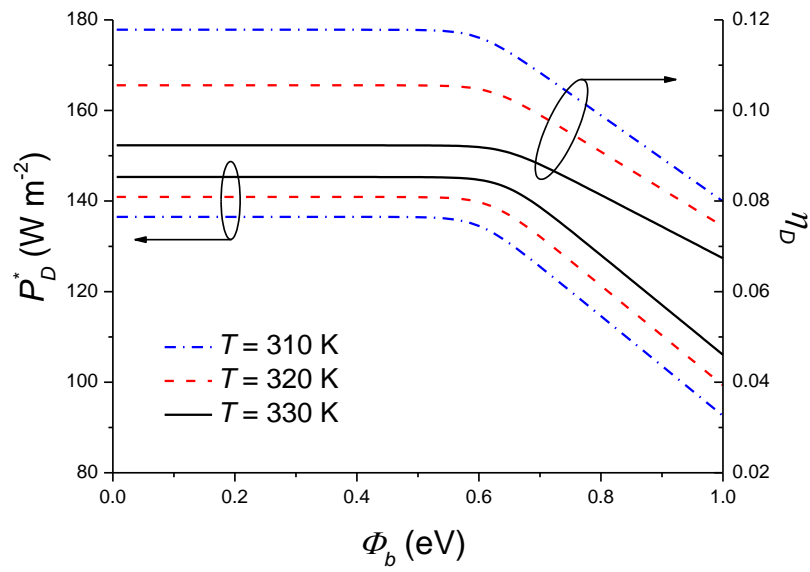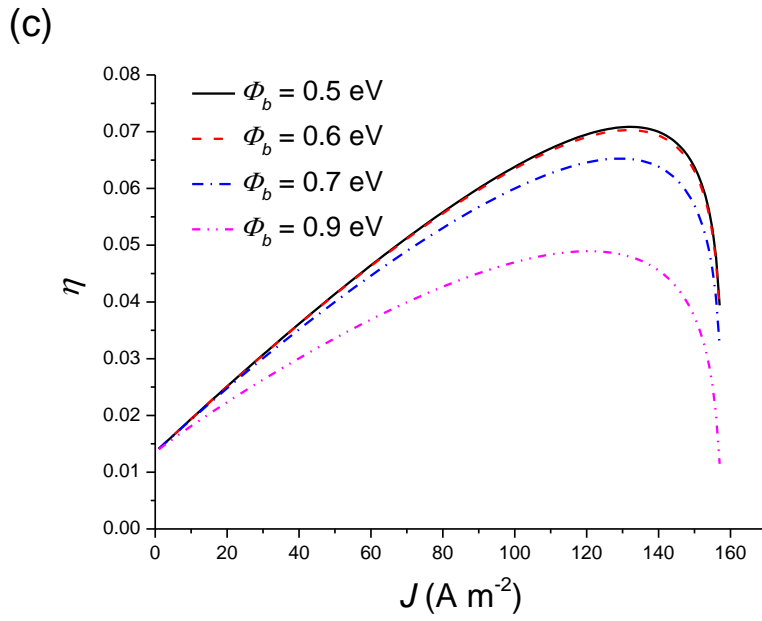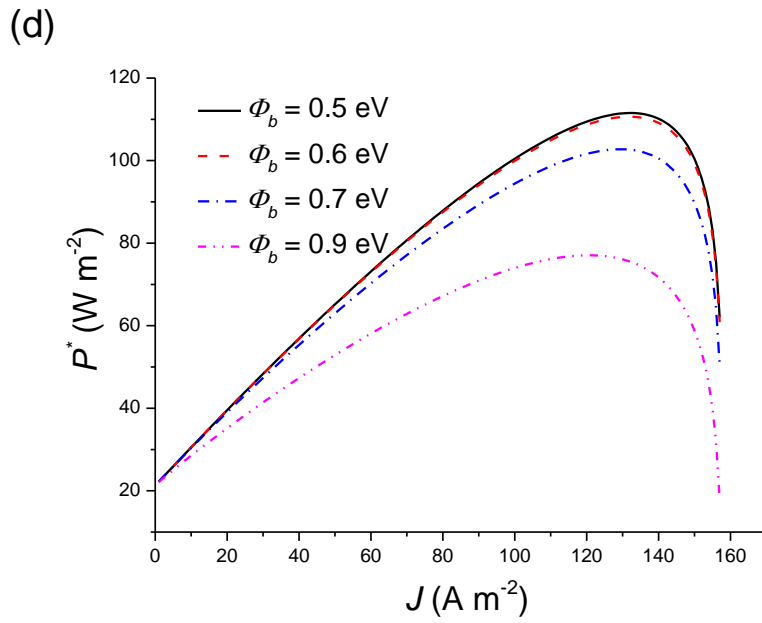
786

787   Fig. 7. Effects of the Schottky barrier on (a) voltage loss, (b) power density and efficiency of DSSC,

788   (c) efficiency of the hybrid system, and (d) power density of the hybrid system.
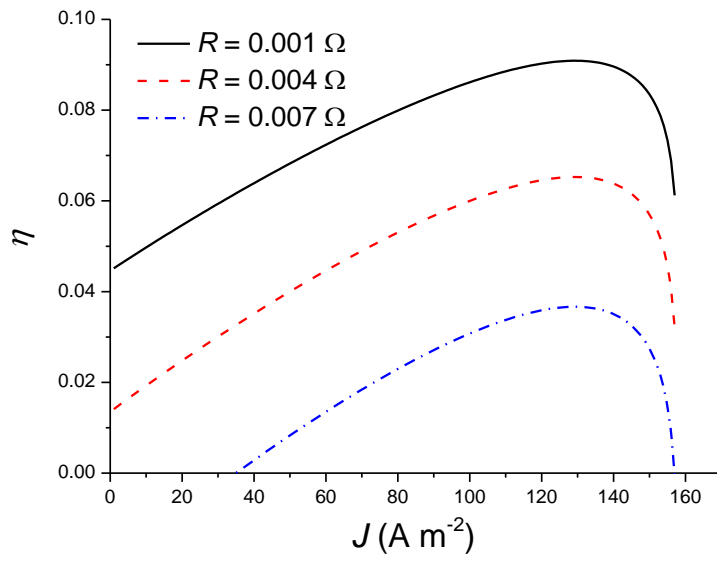
789

Fig. 8.

(a)

791

(b)
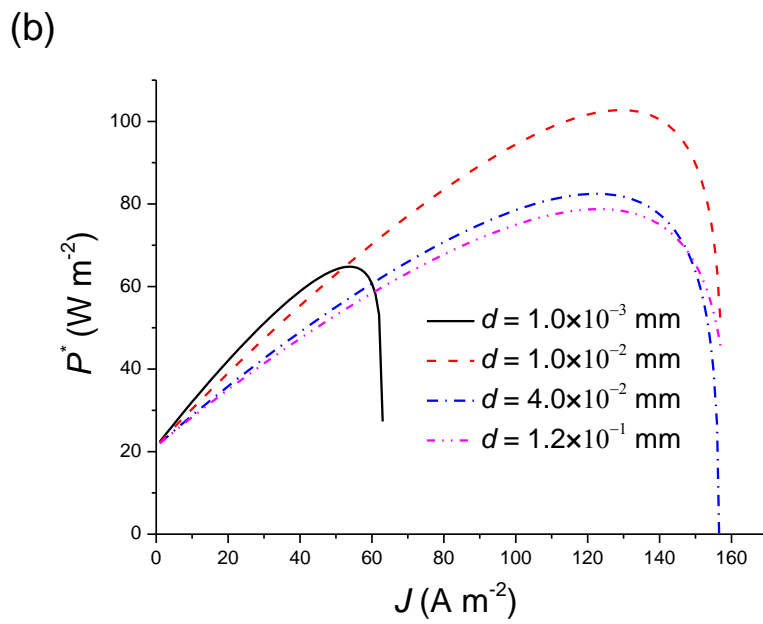
792

793   Fig. 8. Effects of the film thickness on (a) efficiency and (b) power density of the hybrid system.
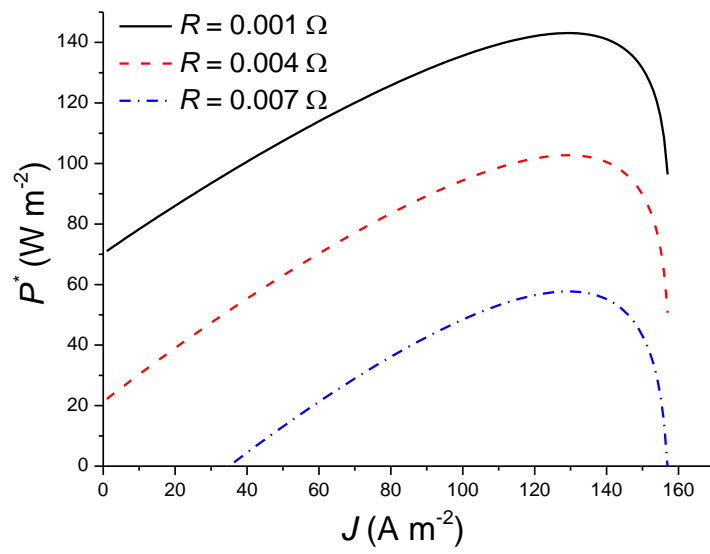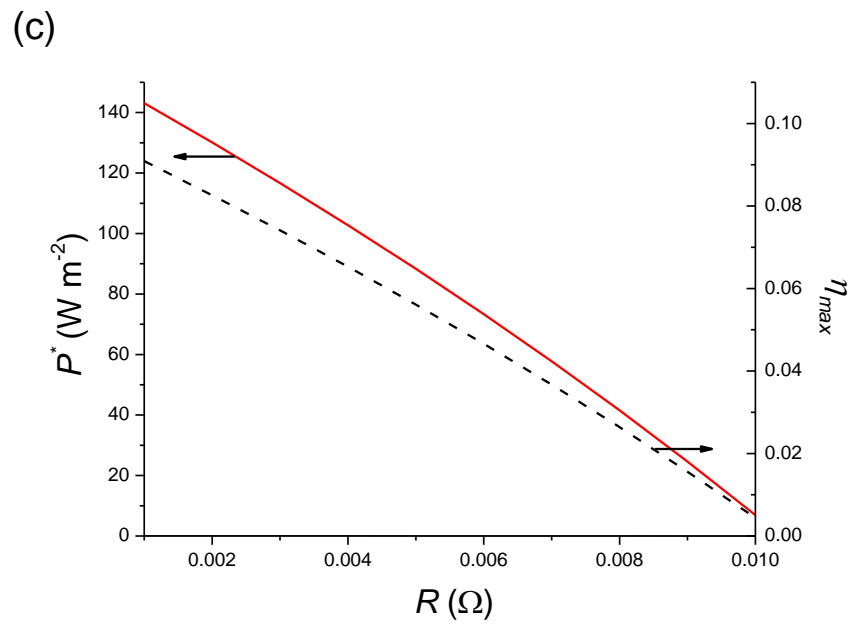
794

795   Fig. 9.

(a)

796

(b)

797

798

(c)

799

800   Fig. 9. Effects of the TREC internal resistance on (a) efficiency, (b) power density, and (c) maximum

801   power density and maximum efficiency of the hybrid system.